Delamination and out-of-plane deformation in drying colloidal suspensions

Paul Lilin, Wim M. van Rees, Mario Ibrahim and Irmgard Bischofberger*

Department of Mechanical Engineering, Massachusetts Institute of Technology, Cambridge, Massachusetts 02139, USA; * Email: irmgard@mit.edu

S1. Vertical deflection of the edge of the deposit

The vertical deflection δ of the edge of the deposit increases with time as the deposit width increases, as shown in Fig. S1. For one second after the time t_f when the liquid region disappears, the vertical deflection continues to increase, reaching a maximum value δ_{max}. The vertical deflection then decreases slightly before becoming constant. The maintained curvature of the deposit after the end of drying indicates that the deformation is plastic.
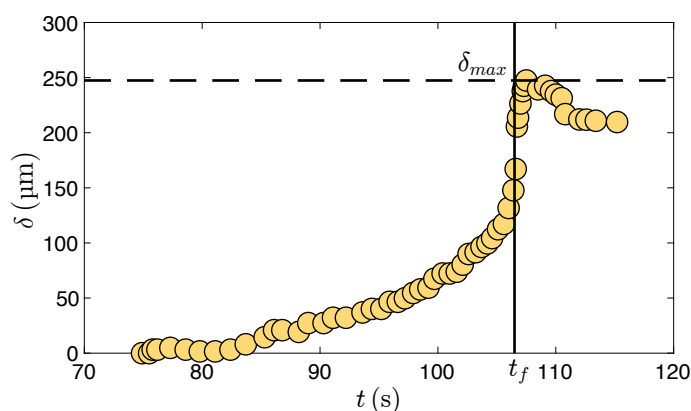

Figure S1: Side-view dynamics. Vertical deflection δ of the edge of the deposit *versus* time since drop deposition t for a drop with initial volume $\Omega_0 = 0.3$ μL and initial particle volume fraction $\phi_0 = 0.12$ drying at relative humidity $RH = 15\%$. The vertical deflection reaches a maximum δ_{max} about one second after the time t_f when the liquid region disappears. δ then decreases slightly to a constant value.

S2. Curvature from side-view imaging and interference microscopy

Side-view imaging provides a convenient way to characterize the large-scale curvature of the deposit expressed as the maximum average curvature $\bar{\kappa}_{max} = 2\delta_{max}/R_0^2$, where δ_{max} is the maximum vertical deflection of the edge of the deposit and R_0 is the radius of the drop. The maximum curvature at the delamination front κ_{max}^* measured using interference imaging and the maximum average curvature $\bar{\kappa}_{max}$ exhibit the same dependence on the average deposit thickness $\bar{h}$, as shown in Fig. S2.
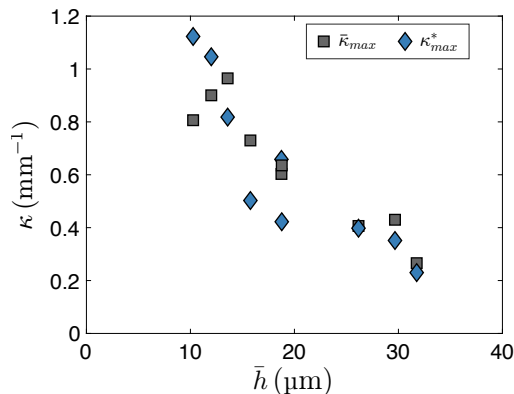

Figure S2: Comparison between curvature from side-view imaging and from interference microscopy. Maximum average curvature $\bar{\kappa}_{max} = 2\delta_{max}/R_0^2$ and maximum curvature at the delamination front κ_{max}^* *versus* average deposit thickness $\bar{h}$. $\bar{\kappa}_{max}$ and κ_{max}^* exhibit the same dependence on $\bar{h}$.

S3. Effect of ionic strength on curvature

We dilute the stock suspension with deionized water, which reduces the salinity and the ionic strength of the suspension by up to 60% from its initial value of $0.04(1)\,\mathrm{mol\,L^{-1}}$. The diluted suspensions are stable over weeks, but the lowered ionic strength could affect the mechanical properties of the deposit. To confirm the generality of the results shown in the manuscript, we conduct additional experiments diluting the suspension with a $0.04\,\mathrm{mol\,L^{-1}}$ NH4Cl salt solution. The deposit curvature is not affected by the change in ionic strength, as shown in Fig.S3.
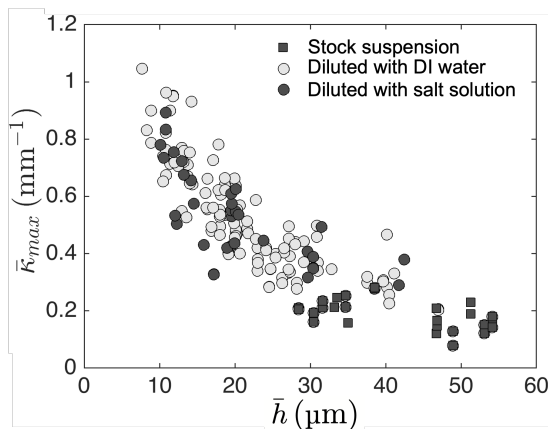

Figure S3: No effect of ionic strength on curvature. The maximum average curvature exhibits the same decrease with the average deposit thickness in suspensions diluted with DI water, which reduces the ionic strength of the suspension, and in suspensions diluted with a salt solution or not diluted.

S4. Modeling and simulation results

Pressure in deposit   For a thin deposit of radius R_0, the local evaporative flux at radius r, $j(r)$, is set by the diffusion of water vapor in the air surrounding the deposit and varies spatially as $j(r) = j_0/2 \left(1 - (r/R_0)^2\right)^{-1/2}$ [1,2], where $j_0 = \dot{\Omega}/(\pi R_0^2)$ and $\dot{\Omega}$ is the volume loss rate for the entire drop. Mass conservation $\nabla \cdot \mathbf{u} = 0$ yields the radial velocity $u_r(r) = j_0 R_0/(2h)\sqrt{R_0^2 - r^2}/r$ and the vertical velocity $u_z(r,z) = j(r)z/\bar{h}$. For the thin deposits that form in our experiments, the in-plane radial flow velocity u_r is a factor $w/\bar{h} = 20$ to 100 larger than the vertical flow velocity u_z, where w is the width and $\bar{h}$ the average thickness of the deposit. To overcome viscous dissipation, this water velocity in the porous deposit requires a pressure gradient given by Darcy's law as $\nabla P(r,z) = -(\mu/k)\mathbf{u}$, where μ is the dynamic viscosity of water and k is the permeability of the deposit. For a deposit of constant thickness, integrating Darcy's law yields

$$
\begin{aligned}
P(r,z) = P(r_l) & \\
- P^* \Bigg(& \operatorname{arctanh}\sqrt{1 - \left(\frac{r_l}{R_0}\right)^2} - \operatorname{arctanh}\sqrt{1 - \left(\frac{r}{R_0}\right)^2} - \sqrt{1 - \left(\frac{r_l}{R_0}\right)^2} + \sqrt{1 - \left(\frac{r}{R_0}\right)^2} \Bigg) \\
& - \frac{P^*}{4}\left(\frac{\bar{h}}{R_0}\right)^2 \left(\left(\left(\frac{z}{\bar{h}}\right)^2 - \frac{1}{3}\right)\left(1 - \left(\frac{r}{R_0}\right)^2\right)^{-1/2} + \epsilon(r,z) \right), \quad (1)
\end{aligned}
$$

where r_l is the radius of the solidification front, $P^* = \left(\mu j_0 R_0^2\right)/\left(k\bar{h}\right)$ is the porous pressure scale associated with flow in the thin deposit, and $\epsilon(r,z)$ is a term that is nonzero only for r close to r_l and R_0 to match the boundary conditions. The pressure at the solidification front $P(r_l)$ is given by the sum of the capillary pressure due to the curvature of the liquid region $\sim \gamma/r_l$ with γ the water-air surface tension, and the pressure due to viscous flows inside the liquid region $\mu_{susp}j_0 R_0^2/h^3$, with μ_{susp} the viscosity of the suspension. Because of the small size of the particles, $k \ll \bar{h}^2$ and the pressure at the solidification front $P(r_l) \ll P^*$; we thus neglect $P(r_l)$ in the following [3,4]. The negative pore pressure in the deposit tends to shrink the deposit: the pore pressure sets an isotropic target strain $\varepsilon_t(r,z) = P(r,z)/Y$, with Y the Young's modulus of the deposit [5]. The target strain is the strain that would release all stresses in the deposit. While the deposit remains adhered to the substrate, it cannot shrink in the in-plane direction leading to tensile stresses that are eventually released by the formation of cracks [4,5]. After the deposit delaminates from the substrate, it is able to shrink and the strain ε gets closer to the target strain ε_t. The out-of-plane deformation induced by gradients in shrinkage in the vertical direction is termed bending, and the out-of-plane deformation induced by gradients in the in-plane direction is termed buckling.

Non-Euclidian plate simulations   To explore both bending and buckling modes of deformation, we conduct non-Euclidian plate simulations where we model the wedge-shaped segment of a drying deposit between two radial cracks as an elastic sheet of constant thickness h subjected to a target strain $\varepsilon_t(r,z) = P(r,z)/Y$. We denote $\mathbf{a}_c$ and $\mathbf{b}_c$ the first and second fundamental forms of the midsurface of the sheet in its current (i.e., strained) configuration. The target strain corresponds to a rest (i.e., unstrained) configuration characterized by the first and second fundamental forms $\mathbf{a}_r$ and $\mathbf{b}_r$, which do not necessarily have to be compatible in this formulation [6,7]. Given a current state $(\mathbf{a}_c, \mathbf{b}_c)$ and a rest state $(\mathbf{a}_r, \mathbf{b}_r)$, the Koiter energy of a monolayer is

$$
E_{\mathrm{ML}} = \frac{1}{2}\int_U \left[\frac{h}{4}\|\mathbf{a}_r^{-1}\mathbf{a}_c - \mathbf{I}\|_e^2 + \frac{h^3}{12}\|\mathbf{a}_r^{-1}(\mathbf{b}_c - \mathbf{b}_r)\|_e^2\right]\sqrt{\det \mathbf{a}_r}\,dxdy, \quad (2)
$$

where we have defined the elastic energy norm as $\|\mathbf{A}\|_e^2 = \alpha \operatorname{Tr}^2(\mathbf{A}) + 2\beta \operatorname{Tr}(\mathbf{A}^2)$, with α and β the plane-stress Lamé parameters [8,9], and where U denotes the domain of the mid-surface parametrization.

We consider a bilayer plate model with two layers, each of thickness $h/2$ and with their own rest metrics $\mathbf{a}_{r1}$ and $\mathbf{a}_{r2}$. It was shown in [9] that the energy of such a bilayer plate in any deformed configuration is equivalent to that of a monolayer with $\mathbf{a}_{r1} = \mathbf{a}_r + \frac{2h}{3}\mathbf{b}_r$ and $\mathbf{a}_{r2} = \mathbf{a}_r - \frac{2h}{3}\mathbf{b}_r$. This equivalence generalizes Timoshenko's bimetallic strip theory to plates [10].

Specifically, we consider isotropically expanding metrics leading to the following rest first fundamental forms:

$$
\mathbf{a}_{r1} = \left(1 + \varepsilon_t^{top}\right)^2 \mathbf{I}, \quad (3)
$$

$$
\mathbf{a}_{r2} = \left(1 + \varepsilon_t^{bottom}\right)^2 \mathbf{I}, \quad (4)
$$

where the target strains are axisymmetrically defined as

$$\varepsilon_t^{top}(r) = \frac{1}{h}\int_0^h \frac{P(r,z)}{Y}\,dz - \frac{1}{2}\frac{P(r,h)-P(r,0)}{Y}, \tag{5}$$

$$\varepsilon_t^{bottom}(r) = \frac{1}{h}\int_0^h \frac{P(r,z)}{Y}\,dz + \frac{1}{2}\frac{P(r,h)-P(r,0)}{Y}, \tag{6}$$

as illustrated in Fig. S4A. For $r < r_l$ we set $\varepsilon_t^{top} = \varepsilon_t^{bottom} = 0$. We vary the ratio of the porous pressure scale and Young's modulus, P^*/Y, and the deposit thickness, h/R_0, and we solve for the shape of the bilayer by discretizing the energy E_{BL} on a triangulated midsurface with 1524 triangles, as shown in Fig. S4B, and using a previously developed solver[9,11]. After the energy has been minimized, the deformed configuration is obtained, as shown in Fig. S4C-D. Sheets in the bending regime exhibit no Gaussian curvature, while sheets in the buckling regime have a region of large positive Gaussian curvature around $r = r_l$. We measure the curvature κ of the deformed configuration along the middle line that bisects the wedge-shaped sheet, as shown in Fig. S4E-F.
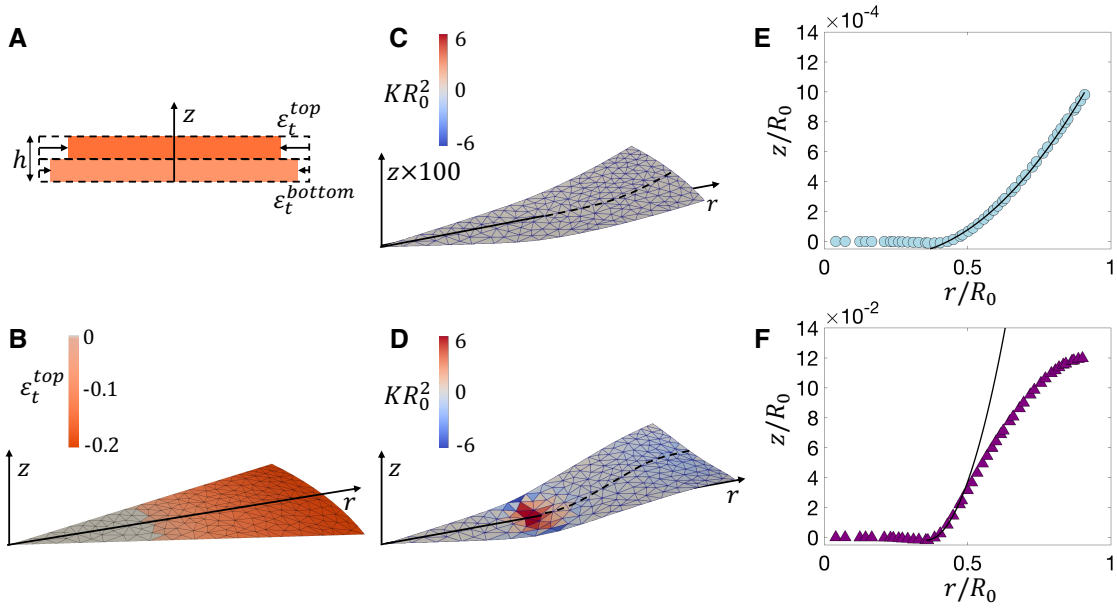

Figure S4: Bending and buckling regimes in simulations. (A) Sketch of the simulation setup. The deposit is modeled as an elastic bilayer in simulations to account for the vertical variation in pore pressure that sets the target strain. Each layer has a thickness $h/2$ and is assigned an isotropic target strain. (B) Simulated sheet before the deformation with the simulation mesh visible. The target strain corresponds to a target strain amplitude $P^*/Y = 0.3$ with $r_l/R_0 = 0.4$. (C) Simulated deformed configuration for a sheet in the bending regime with thickness $h/R_0 = 15 \cdot 10^{-3}$ and target strain amplitude $P^*/Y = 0.3$ with $r_l/R_0 = 0.4$. The color indicates the Gaussian curvature K scaled by R_0^2. The vertical deflections are magnified by a factor 100. The dashed line denotes the midline of the sheet. (D) Simulated deformed configuration for a sheet in the buckling regime with thickness $h/R_0 = 3 \cdot 10^{-3}$ and target strain amplitude $P^*/Y = 0.3$ with $r_l/R_0 = 0.4$. The deformed sheet has a non-zero Gaussian curvature K and reaches vertical deflections 100 times larger than the sheet in (C). (E) Deflection profile of the midline of the sheet in the bending regime. The line represents a parabolic fit for $r > r_l$ from which the curvature κ is obtained. (F) Deflection profile of the midline of the sheet in the buckling regime. The line represents a parabolic fit for $r > r_l$ and $z/R_0 < 0.006$ from which the curvature κ is obtained.

S5. Target curvature is attained in the bending regime

Vertical flows in the deposit result in a target curvature $\kappa_t \sim \mu j_0/(kY)$. This target curvature can be expressed in terms of simulation units as $\kappa R_0 \sim (P^*/Y)(h/R_0)$. As shown in Fig. S5, the simulations in the bending regime exhibit the expected curvature.
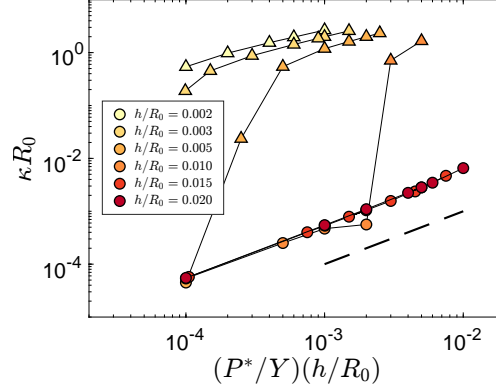

Figure S5: Simulations recover the expected target curvature κ_t in the bending regime. Normalized curvature κR_0 of the midline of the sheet close to r_l *versus* normalized target curvature $(P^*/Y)(h/R_0) \sim \kappa_t R_0$. The dashed line represents a slope of 1. Simulations in the bending regime are represented by circles and simulations in the buckling regime are represented by triangles. The simulations in the bending regime exhibit a curvature $\kappa = \kappa_t$.

S6. Effect of imposing a maximum strain on buckling curvature in simulations

To test whether the localized buckling curvature observed in simulations depends on the overall target strain or only on the local target strain, we perform additional simulations where the target strain is limited to -0.05. The resulting deflection profile deviates from that without a maximally negative target strain at large r/R_0, as shown in Fig. S6A. The localized curvature, however, is not affected, as shown in Fig. S6A and B. The buckling curvature is thus locally set by the radial variation in the target strain.
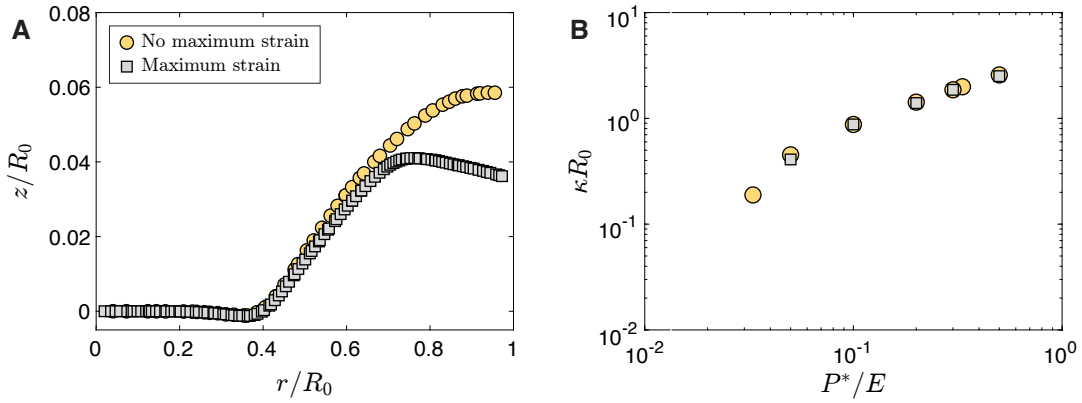

Figure S6: Buckling occurs locally. (A) Deflection profile of the midline of the sheet for two simulations with $h/R_0 = 3 \cdot 10^{-3}$, $P^*/E = 0.1$ and $r_l/R_0 = 0.4$. Setting a maximally negative target strain of -0.05 yields the profile shown in gray squares. The profile with a maximally negative target strain of -0.05 (gray squares) and the original profile (orange circles) are identical for r/R_0 close to r_l/R_0 but deviate when the maximally negative target strain is reached at $r/R_0 \approx 0.6$. (B) Normalized curvature κR_0 of the midline of the sheet close to r_l *versus* target strain amplitude P^*/E for simulations in the buckling regime with $h/R_0 = 3 \cdot 10^{-3}$ and $r_l/R_0 = 0.4$.

5

Caption for Movie S1. Drying and out-of-plane deformation of a colloidal suspension drop. Simultaneous bottom-view interference microscopy video (left) and side-view video (right) of a drop of a silica particle suspension with initial volume $\Omega_0 = 0.3$ μL and initial particle volume fraction $\phi_0 = 0.18$ drying on a glass slide at a relative humidity of $RH = 49\%$. The black and white interference fringes in the bottom-view video indicate that the deposit delaminates from the substrate. The drop deposition diameter is $2R_0 = 1780$ μm. The video is accelerated 5 times.

Caption for Movie S2. Deposit curvature is set locally. Animated version of Fig. 3. The curves that represent the location of the upper interface z_{top} of the solid deposit at different times are superposed by a rotation and a translation, demonstrating that the deposit only deforms in a small region close to the delamination front, and then maintains its curvature. The drop has an initial volume $\Omega_0 = 0.3$ μL, an initial particle volume fraction $\phi_0 = 0.14$ and dries at relative humidity $RH = 14\%$. The times range from 23 to 58 s.

Caption for Movie S3. Effect of particle volume fraction on deposit curvature Side-view videos of drops with initial volume $\Omega_0 = 0.3$ μL and initial particle volume fractions (from left to right) $\phi_0 = 0.08$, $\phi_0 = 0.18$ and $\phi_0 = 0.23$ drying at relative humidity $RH = 54\%$. The video is played in real time and the scale bar represents 1 mm.

References

[1] A.-M. Cazabat and G. Guéna, *Soft Matter*, 2010, **6**, 2591.

[2] J. Crank, *The Mathematics of Diffusion*, Oxford Univ. Press, 1975.

[3] C. N. Kaplan and L. Mahadevan, *J. Fluid Mech.*, 2015, **781**, R2.

[4] P. Lilin and I. Bischofberger, *Langmuir*, 2022, **38**, 7442–7447.

[5] L. Goehring, A. Nakahara, T. Dutta, S. Kitsunezaki and S. Tarafdar, *Desiccation Cracks and Their Patterns: Formation and Modelling in Science and Nature*, John Wiley & Sons, 2015.

[6] P. G. Ciarlet, *J. Elasticity*, 2005, **78**, 1–215.

[7] E. Efrati, E. Sharon and R. Kupferman, *J. Mech. Phys. Solids*, 2009, **57**, 762–775.

[8] C. Weischedel, A. Tuganov, T. Hermansson, J. Linn and M. Wardetzky, *Construction of Discrete Shell Models by Geometric Finite Differences*, Fraunhofer ITWM Technical Report 220, 2012.

[9] W. M. van Rees, E. Vouga and L. Mahadevan, *Proc. Natl. Acad. Sci. U.S.A.*, 2017, **114**, 11597–11602.

[10] S. Timoshenko, *J. Opt. Soc. Am., JOSA*, 1925, **11**, 233–255.

[11] W. M. van Rees, E. A. Matsumoto, A. S. Gladman, J. A. Lewis and L. Mahadevan, *Soft Matter*, 2018, **14**, 8771–8779.